

Synthesis of Cu/CeO_{2-x} Nanocrystalline Heterodimers with Unique Interfacial Active Sites to Promote CO₂ Electroreduction

Seyedeh Behnaz Varandili^a, Jianfeng Huang^a, Emad Oveisi^b, Gian Luca De Gregorio^a, Mounir Mensi^c, Michal Strach^a, Jan Vavra^a, Chethana Gadiyar^a, Arghya Bhowmik^d, Raffaella Buonsanti^{a}*

^a Laboratory of Nanochemistry for Energy (LNCE), Institute of Chemical Sciences and Engineering (ISIC), École Polytechnique Fédérale de Lausanne, CH-1950 Sion, Switzerland.

^b Interdisciplinary Center for Electron Microscopy (CIME), École Polytechnique Fédérale de Lausanne, CH-Lausanne, Switzerland.

^c Institute of Chemical Sciences and Engineering (ISIC), École Polytechnique Fédérale de Lausanne, CH-1950 Sion, Switzerland.

^d Department of Energy and Conversion Storage, Technical University of Denmark (DTU), Lyngby, 2800 Kgs, Denmark

*Address correspondence to: raffaella.buonsanti@epfl.ch

Abstract

Synergistic effects at metal/metal oxide interfaces often give rise to highly active and selective catalytic motifs. So far, such interactions have been rarely explored to enhance the selectivity in the electrochemical CO₂ reduction reaction (CO₂RR). Herein, Cu/CeO_{2-x} heterodimers (HDs) are synthesized and presented as one of the prime examples where such effects promote CO₂RR. A colloidal seeded-growth synthesis is developed to connect the two highly mismatched domains (Cu and CeO_{2-x}) through an interface. The Cu/CeO_{2-x} HDs exhibit state-of-the-art selectivity towards CO₂RR (up to ~80%) against the competitive hydrogen evolution reaction (HER) and high faradaic efficiency for methane (up to ~54%) at -1.2 V_{RHE}, which is ~5 times higher than that obtained when the Cu and CeO_{2-x} nanocrystals are physically mixed. Operando X-Ray absorption spectroscopy along with other ex-situ spectroscopies evidences the partial reduction from Ce⁴⁺ to Ce³⁺ in the HDs during CO₂RR. A Density Functional Theory (DFT) study of the active site motif in reducing condition reveals synergistic effects in the electronic structure at the interface. The proposed lowest free energy pathway utilizes O-vacancy site with intermediates binding to both Cu and Ce atoms, a configuration which allows to break the CHO*/CO* scaling relation. The suppression of HER is attributed to the spontaneous formation of CO* at this interfacial motif and subsequent blockage of the Cu-sites.

Keywords: synthesis design; interfaces; colloidal nanocrystals; electrochemical CO₂ reduction, copper, ceria

1. INTRODUCTION

Electrochemical CO₂ conversion offers the unique promise to combine CO₂ utilization and storage of renewable energies in one process.^{1,2} Nevertheless, its practical implementation is limited by a few challenges including to design catalysts which selectively promote the electrochemical CO₂ reduction reaction (CO₂RR) over the competing hydrogen evolution reaction (HER) towards the desired target products, such as energy-dense hydrocarbons and alcohols.^{1,2} Copper still remains the only suitable monometallic electrocatalyst able to produce C₂₊ products, yet improvements are still required in terms of activity and selectivity.¹⁻³ The performance of Cu are intrinsically limited by the scaling relations between the adsorption energies of the various reaction intermediates on the metallic surfaces.^{4,5} Nanostructuring,⁶⁻⁹ shape control,^{8,10,11} compositional tuning^{12,13,14} and defect engineering¹⁵ are some of the strategies adopted so far to modulate the intrinsic activity and selectivity of Cu metal. Theoretical investigations suggest that truly bi-functional active sites are desirable to effectively break the scaling laws, resulting in superior performance for CO₂RR.⁴

Metal/ceria interfaces are identified as highly active and selective catalytic sites in CO₂ hydrogenation and CO oxidation reactions, which share similar oxygen-containing intermediates with the CO₂RR.¹⁶⁻²⁰ Yet, to the best of our knowledge, such interfacial synergic effects have limited to only one study for CO₂RR.²¹ In the latter, Au/CeO_x and Ag/CeO_x interfaces were shown to promote activity and selectivity of the metallic domain for the electrochemical conversion of CO₂ to CO through stabilization of the *COOH reaction intermediate.²¹ While Cu-doped ceria has been investigated in an interesting recent work²², no studies of the Cu/CeO_x interface for electrochemical CO₂ conversion have been reported so far. It is possible that metal/metal oxide interfaces are still underexplored in electrocatalysis due to the lack of charge conductivity in metal

oxides in the form of bulk powders, a limit which can be overcome by using thin films or nanostructured oxide domains.^{21–25}

Here, we report the synthesis of novel Cu/CeO_{2-x} nanocrystalline heterodimers (HDs) and the study of their catalytic behaviour towards CO₂RR. By using a colloidal seeded-growth approach, we overcome the synthetic challenge imposed by the high lattice-mismatch between Cu and CeO_{2-x}. In colloidal chemistry, the presence of ligands and of solid/liquid interfaces contributes to modulate the interfacial energies, thereby allowing the formation of heterostructures to occur even in highly mismatched system, something which would be more challenging by traditional deposition techniques such as molecular beam epitaxy and chemical vapor deposition.^{26,27} We show that the formation of the interface in the Cu/CeO_{2-x} HDs gives rise to up to 80% faradaic efficiency for carbon products, including up to 54% selectivity for methane at -1.2 V_{RHE}. These values are around ~5 times higher than those obtained with a physical mixture of isolated Cu and CeO_{2-x} nanocrystals (NCs) of similar sizes under the same operational conditions, thus highlighting the important role played by the intimate bonding at the interface. Operando X-ray absorption near-edge (XANES) and ex-situ X-Ray photoelectron, Raman and UV-Vis spectroscopies indicate the partial reduction of ceria during CO₂RR. DFT calculations highlight the presence of unique catalytic motifs which enable bidentate adsorption at both the Cu and the CeO_{2-x} O-vacancy site which create an opportunity for reaction engineering beyond scaling relationship limitations. Future studies involving different metal oxide domains will allow to explore further this concept in CO₂RR.

2. EXPERIMENTAL SECTION

2.1 Chemicals. Cerium(III) nitrate hexahydrate ($\text{Ce}(\text{NO}_3)_3 \cdot 6\text{H}_2\text{O}$, 99%), copper(I) acetate (or CuOAc , 97%), copper(I) bromide (CuBr , 99.999%), trioctylphosphine oxide ($\{\text{CH}_3(\text{CH}_2)_7\}_3\text{PO}$, or TOPO), tetradecylphosphonic acid ($\text{CH}_3(\text{CH}_2)_{13}\text{P}(\text{O})(\text{OH})_2$) or TDPA, 97%), oleic acid ($\text{C}_{17}\text{H}_{33}\text{CO}_2\text{H}$ or OLAC, 90%), 1-octadecene ($\text{C}_{18}\text{H}_{36}$ or ODE, 90%), oleylamine ($\text{C}_{17}\text{H}_{33}\text{NH}_2$ or OLAM, 70%), and 1-octanoic acid ($\text{C}_7\text{H}_{15}\text{CO}_2\text{H}$ or OCAC, 90%) were all purchased from Sigma-Aldrich and used as received.

2.2 Synthesis

Synthesis of Cu/CeO_{2-x} HDs. As a general procedure, 0.5 μmol of CeO_{2-x} seeds (Figure S1) in 10 mL of ODE were mixed in a 25 mL three-necked flask. The mixture was degassed under dynamic vacuum for 20 min at 130°C, after which it was heated under N_2 flow to 300°C. After 5 min equilibration time, a precursor solution containing CuOAc (0.1 mmol, 0.2 mmol and 0.4 mmol, 0.8 mmol for copper domain size of 15 nm, 24 nm, 36 nm and 54 nm respectively), 0.6 mmol of OLAM and 0.6 mmol of OLAC in 2.4 mL of degassed ODE was added to the stirring mixture at a rate of 0.18 mL/min using a syringe pump (Figure S2). Upon the addition of this precursor solution, the reaction mixture slowly turned from colourless to brown. After injection of 0.7 mL of the solution to the reaction mixture, the injection was stopped and the mixture was allowed to cool to room temperature by removing the heating mantle. The HDs were then extracted and purified by repeated washing / centrifugation cycles; the HDs were handled inside a N_2 glovebox to avoid oxidation of Cu prior to electrochemistry. Anhydrous ethanol was added to the reaction mixture at room temperature and the mixture was transferred to centrifugation vials; the particles were collected by centrifugation at 6000 rpm for 15 min. The precipitate was washed twice with ethanol to remove residual amounts of precursor and surfactant. Finally, the HDs were re-dispersed

in hexane. The yield was calculated using the following equation by performing a statistical analysis on 72 particles in the TEM images. ($\frac{100 \times \text{No. of HDs}}{\text{No. of isolated seeds} + \text{No. of HDs}} = 80 \%$). Details on the formation mechanism of the HDs will be discussed in a different publication.

Preparation of the Cu-CeO₂ physical mixture. CeO_{2-x} and Cu NCs were synthesized separately and the concentrations of their stock solutions (in hexane) determined by ICP. Physical mixtures were then prepared by mixing the two NCs in a volumetric ratio such that the relative Ce and Cu concentrations in the mix mimicked those ratios found in the HDs.

2.2 Characterization

X-ray diffraction (XRD). X-ray diffraction was carried out on a Bruker D8 Advance diffractometer with a Cu K_α source equipped with a Lynxeye one-dimensional detector. The diffractometer operated at 40 kV and 40 mA with a Cu K_α source with wavelength of $\lambda = 1.54 \text{ \AA}$. Rietveld analysis was performed using Topas. Patterns were fitted using CeO_{2-x} and Cu structures available in the PDF 4+ ICDD 2018 database. The alumina standard NIST SRM1976b was employed to determine instrumental peak broadening for size analysis. The domain sizes were determined from the volume-weighted mean column-height using the macro LVol_FWHM_CS_G_L in Topas.

Thermogravimetric analysis (TGA). In order to determine the loading of CeO_{2-x} NC seeds, 60 μL of the solution was deposited in an aluminium pan, which was introduced into a TGA Q500 with the flow of air maintained at 15 mL/min. The sample was heated to 600°C with a heating ramp of 10°C/min. Based on the final weight, the concentration of CeO_{2-x} solution was calculated.

Inductively coupled plasma-optical emission spectrometry (ICP-OES). ICP-OES was performed on Agilent 5100 model to determine the Ce and Cu concentration in Cu/CeO_{2-x} HDs and Cu-CeO₂.

x physical mixture and individual Cu NCs. For the digestion of the solutions, upon evaporation of the hexane, 285 μ L of each HNO₃(70%) and H₂O₂(35%) was added to 100 μ L of the as-synthesized NCs solutions and left overnight to ensure complete digestion of the samples. Following this step, 9.430 mL of Milli-Q water was added to the solution to reach the 2% acid content needed for the analysis. 5 standard solutions of Ce and Cu were prepared to obtain the calibration curve which was used to determine the concentrations of the digested solutions.

X-ray photoelectron spectroscopy (XPS). XPS was performed using VersaProbe II from Physical Electronics. Analysis was carried out using a monochromatic Al K α X-ray source operating at 25 W with a beam size of 100 μ m. The spherical mirror analyzer was set at 45° take-off angle with respect to the sample surface. The binding energy of the spectra were calibrated by setting the C-C bound of the C 1s peak at 284.8 eV. In the fitting the FWHM of each component was limited to 3.5 eV and the fitting was mathematically optimized to maximize R-squared between the fit and the signal.

Raman spectroscopy. Raman spectroscopy was performed using a Renishaw inVia Raman microscope, where the focused excitation light is collected in a back-scattering configuration. The samples were drop-cast on glassy carbon and loaded onto a translational stage of a Leica microscope equipped with a 100x objective lens, and the excitation laser is a laser diode of 633 nm at 5% power. Lower wavelengths of the excitation laser were not employed because of the strong fluorescence background from metallic copper. The spectra were collected from 250 cm⁻¹ to 900 cm⁻¹ with a 25-minute acquisition time. The spectral positions were calibrated by the characteristic Si phonon peak at 520.7 cm⁻¹.

Electron microscopy. Samples were drop-casted on a copper TEM grid (Ted Pella, Inc.) prior to imaging. BF-TEM images were obtained with a FEI Tecnai Spirit at 120 keV. HAADF-STEM imaging and energy dispersive X-ray analysis (EDX) were performed on a FEI Tecnai Osiris transmission electron microscope in scanning mode at an accelerating voltage of 200 kV. This microscope is equipped with a high brightness X-FEG gun, silicon drift Super-X EDX detectors and a Bruker Esprit acquisition software. Aberration-corrected (Cs) high-resolution S/TEM imaging were performed on a FEI Titan Themis 60-300 at an accelerating voltage of 200 kV.

2.3 Electrocatalytic measurements

The electrocatalytic testing was performed in a custom made electrochemical flow cell (Figure S3). Glassy-carbon plate electrodes (Type 2, Alfa Aesar) with a surface area of 2.5 cm x 2.5 cm were used as substrates. They were polished using Milli-Q water slurries of 1 μm diamond (Bioanalytical Systems, Inc.) and 50 nm gamma alumina (Bioanalytical Systems, Inc.) on polishing pads. The plates were rinsed with Milli-Q water, sonicated in Milli-Q water for 10 minutes, and blown dry with nitrogen. Cu NCs, Cu/CeO_{2-x} HDs and Cu-CeO_{2-x} mix, were drop-cast on the substrate from toluene suspensions, giving mass loadings of 8, 15, 25 and 35 μg . Electrochemical measurements were performed using a Biologic SP-300 potentiostat. Platinum foil was employed as the counter electrode and a Ag/AgCl reference electrode (leak free series from Innovative Instruments, Inc.) was used. Voltages were converted to the RHE scale. Ambient-pressure CO₂ electrolysis was carried out in a custom-made gas-tight electrochemical cell made of poly(methylmethacrylate) and fitted with Buna-N O-rings. The configuration of the electrochemical cell was such that the working electrode sat parallel with respect to the counter electrode to ensure a uniform potential distribution across the surface. The geometric surface area for both of the electrodes was 1 cm². Each of the compartments in this cell were filled with

electrolyte (0.1 M KHCO_3 solution, 2.1 mL in each half). A Selemion AMV anion-exchange membrane was used to separate the anodic and cathodic compartments. The electrolyte solution was prepared by sparging a 0.05 M K_2CO_3 solution with CO_2 for 1 hour. Before CO_2 electrolysis was conducted, the electrolyte in the cell was sparged with CO_2 for at least 15 min. During electrolysis, CO_2 was constantly bubbled through the electrolyte at a flow rate of 5 sccm to prevent depletion of CO_2 in the electrolyte and to enable continuous analysis of gaseous products using a gas chromatograph. The flow rate of CO_2 was controlled with a mass flow-controller (Bronkhorst), and the gas was first humidified with water by passing it through a bubbler to minimize evaporation of the electrolyte. Calibration of the gas chromatograph was performed using calibration gas standards from Carbogen. CO , CH_4 , C_2H_4 and C_2H_6 were all calibrated from calibration mixtures at five different concentrations: 50, 100, 250, 500 and 1000 ppm. H_2 was likewise calibrated using 500, 1000, 5000, 10000 ppm of H_2 balanced in nitrogen. After passing through the cell, CO_2 was flowed directly into the gas-sampling loop of the GC for online gaseous product analysis, which was carried out every 10 min. For all experiments, electrolysis was carried out for 80 min with gas analysis recorded at 10 min intervals.

2.4 Operando X-Ray Absorption Spectroscopy

X-ray absorption operando experiments were performed at the SuperXAS beamline at the SwissLight Source synchrotron. All reported spectra were recorded in fluorescence mode at an incident angle of 45 degrees. A Si(111) monochromator was used to condition the beam from a bending magnet. The beam spot was focused using a toroidal mirror to approximately $60 \times 120 \mu\text{m}$, to match the shape of the SiN window on the sample substrate. Fluorescence XANES spectra were acquired using a silicon drift detector available at the beamline with a time resolution of 8 minutes. The data were treated using Demeter software package. The references that were used in the linear

combination fitting of the Ce L3-edge were: Ce (IV) - CeO₂ 99.9% powder <5µm (CAS: 1306-38-3), and Ce (III) - cerium acetate hydrate 99.99% powder (CAS: 206996-60-3). The powders were co-grinded with BN fine powder in ratios according to 2.5 attenuation length, and pressed into pellets. To carry out the operando spectroscopy in fluorescence mode, a gas-tight electrochemical cell was developed. 200 µm thick Si TEM chips with SiN windows (50-200 nm thick) and up to 500x500 µm in size (Figure S4) were used as substrate for the catalyst. A monolayer of the nanocrystals was deposited on the chip so to cover the entire SiN window area in order to assure that the majority of the particles take part in the reaction. Electrical contact was achieved by a thin layer of carbon coating micro-patterned on the window area, and a Pt thin layer lead. The electrolyte pressure was controlled to avoid stationary pressure.

2.5 DFT Calculations

Density functional theory based simulations for model Cu/CeO_{2-x} system is done with VASP²⁸ package and ASE²⁹ simulation environment. RPBE³⁰ exchange correlation functional and a wavefunction cutoff of 400 eV is used. We have used Hubbard U of 4.5 eV for the Ce f-states. The Brillouin zone is sampled only at the gamma point, as the simulation cell is large. The model system consist of Ce₆O₁₃ cluster on $4\sqrt{3} \times 4\sqrt{3}$ Cu(111) surface with four atomic layers and 192 Cu atoms – of which bottom two layers are kept fixed at bulk structure. The Ce₆O₁₃ cluster is modified based on hydrogenation, vacancy formation and adsorbed CO₂RR intermediates. Zero point energy and free energy contributions at finite temperature for adsorbates and gas molecules are estimated using ideal gas model and harmonic approximation to the vibrational modes following the method described in details elsewhere³¹. The change in free energy under an applied potential for elementary proton transfer steps is calculated using the computational hydrogen electrode (CHE) model³², which links the change in reaction free energy linearly to the applied

potential in the reversible hydrogen electrode scale (V_{RHE}). Change in free energy of each elementary reaction step is evaluated from electronic energy of the system before and after the reaction step, reference molecules' free energy and temperature corrections for the adsorbates involved. Methods for stability estimation of structures under applied potential and reaction thermodynamics analysis follows from reference ³¹. Electronic energies, temperature corrections and molecular structures are provided in the supplementary information (Tables S2, S3, S4).

3 RESULTS AND DISCUSSION

In a typical synthesis of the Cu/CeO_{2-x} HDs, pre-formed CeO_{2-x} NCs of 9 nm are used as nucleation seeds for the growth of the Cu domain (Figure S1). In order to promote heterogeneous nucleation, the Cu molecular precursor (copper(I) acetate, CuOAc) is injected drop-wise so to maintain the Cu monomer concentration below the supersaturation limit and to avoid homogeneous nucleation (Figure S2). Different parameters were optimized to synthesize the HDs, including temperature, [Cu precursor]/[seed] and the [Cu precursor]/[ligand] ratios.

Figure 1 gives an overview of the structural and compositional analysis of the Cu/CeO_{2-x} HDs obtained by injecting different amount of Cu precursor in the reaction solution. In the bright-field transmission electron microscopy (TEM) images (Figure 1a-d), each 9 nm spherical CeO_{2-x} domain is coupled with one Cu domain (HD yield = 80%).

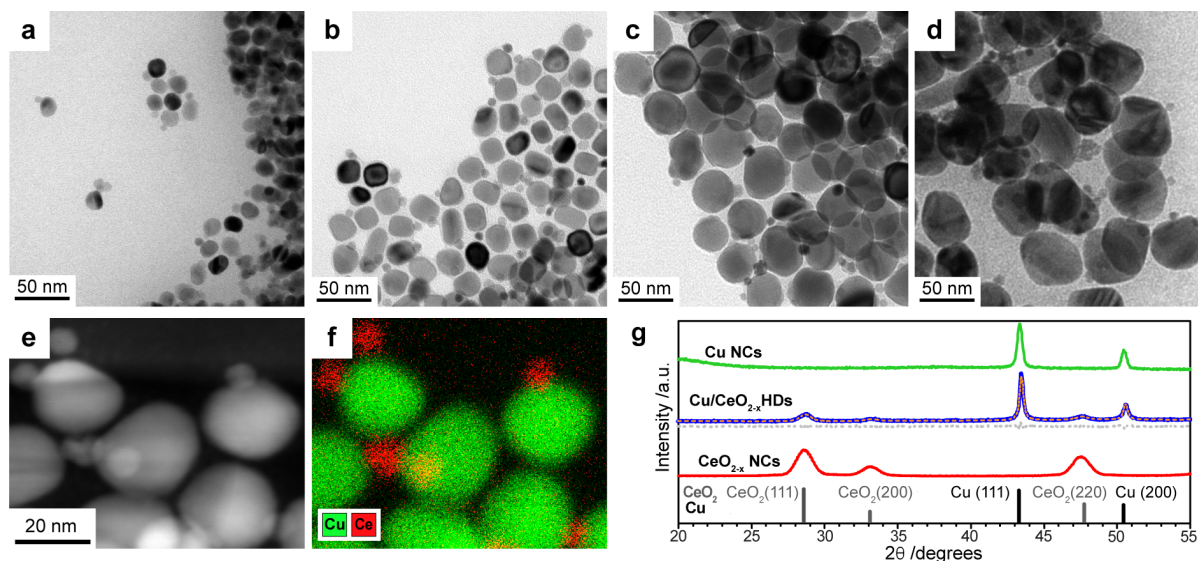


Figure 1. a) Bright-field TEM image of Cu/CeO_{2-x} HDs formed by injection of: a) 0.1 mmol, b) 0.2 mmol c) 0.4 mmol and d) 0.8 mmol of CuOAc. The sizes of the Cu domain are 15 nm, 24 nm, 36 nm and 54 nm, respectively. e, f) HAADF-STEM image with the corresponding EDX elemental maps of Cu and Ce in the Cu(24nm)/CeO_{2-x} HDs. f) Representative XRD pattern of the HDs from Cu(24nm)/CeO_{2-x} HDs and individual ceria and copper NCs with similar mean particle size to those in Cu(24nm)/CeO_{2-x} HDs. Rietveld analysis was performed on the pattern of the Cu/CeO_{2-x} HDs, the profile fitting overlaps the experimental data as an orange dashed line, the difference is reported at the bottom of the pattern. Reference patterns for ceria (PDF #04-0593) and copper (PDF #04-0836) are reported at the bottom of the graph.

The distribution of Cu and ceria in the HDs was confirmed by high-angle annular dark-field scanning transmission electron microscopy (HAADF-STEM, Figure 1e) with the relative area-selective energy-dispersive X-ray (EDX) spectroscopy map (Figure 1f). The phase composition of the Cu/CeO_{2-x} HDs was investigated by X-Ray Diffraction (XRD) analysis whose results are reported in Figure 1g and Figure S5 along with the patterns of individual ceria and copper NCs. The profiles of the individual CeO_{2-x} and Cu NCs were found to be consistent with the standard

patterns of fluorite ($Fm\bar{3}m$) and with the FCC structure, respectively. The XRD patterns of the Cu/CeO_{2-x} HDs contains the characteristic features of both the CeO_{2-x} seeds and the metallic Cu phase without any shifting in the position of the peaks, thereby excluding the possibility of doping. The quantitative Rietveld refinement analysis indicates that the Cu(24nm)/CeO_{2-x} HDs are formed of 84% copper and 16% ceria with approximate sizes of 27 nm and 10 nm, respectively, in very good agreement with the data from TEM.

Because of the significant lattice mismatch between the CeO_{2-x} ($a = b = c = 5.411 \text{ \AA}$) and the Cu ($a = b = c = 3.610 \text{ \AA}$), only partial “wetting” of Cu on the CeO_{2-x} seeds is energetically allowed and therefore the heterodimers formation is favoured over a core-shell configuration. This is reminiscent of the Volmer-Weber mechanism of growth of secondary islands on mismatched substrates through heteroepitaxial deposition techniques.²⁶ Considering the large mismatch, a mechanism for strain relaxation must be in place for heterogeneous nucleation to occur. Aberration-corrected high-resolution electron microscopy provided a more detailed picture of the structure of the HDs (Figure 2, Figures S6 and S7).

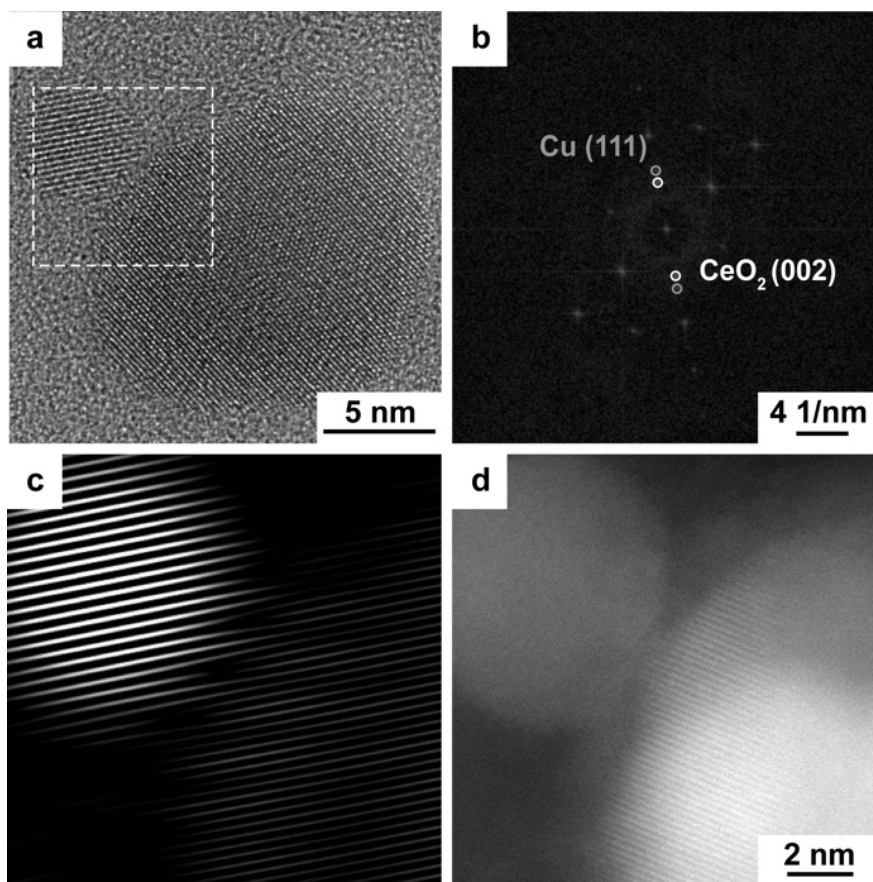


Figure 2. a) HR-TEM image of one representative Cu/CeO_{2-x} HD, b) FFT diffractogram of the interfacial region, c) inverse FFT (pseudo-dark field image) and d) HR-STEM image of the interfacial region (a). Reciprocal plane spacing on the FFT correspond to the (111) planes of a copper crystal oriented along a $[1\bar{1}0]$ direction, and to the (002) plane of CeO₂.

First of all, the lattice spacing from the FFT analysis on the whole HD (Figure S6) and on the interfacial region (Figure 2b) is consistent with CeO_{2-x} in the smaller domain and Cu in the larger domain of the HDs. A straightforward epitaxial relationship at the interface is missing, however the pseudo dark-field image (Figure 2c) indicates a possible epitaxial connection between the ceria and the copper domain along the (111) and (002) crystallographic planes of copper and ceria, respectively. There is also evidence for distortion in the copper lattice in proximity of the ceria

domain, which results in a 20% deviation from the standard copper (111) spacing in its $[1\bar{1}0]$ zone axis. Similar distortion of the Cu domain lattice is found in other but not in all the analysed HDs (Figure S7), meaning that lattice strain is not uniform across the HDs. The HR-STEM image (Figure 2d) is consistent with the picture of an amorphous interface with the possibility of some epitaxial connections between the two domains.

The catalytic performance of the Cu/CeO_{2-x} HDs towards the CO₂RR were compared against a Cu-CeO_{2-x} physical mixture (Cu-CeO_{2-x} mix) and isolated Cu NCs with similar size to the Cu domain in the HDs to investigate the role of the Cu/CeO_{2-x} interface, which is the main goal of this study.

At first, the HDs with the different Cu domain sizes were tested at -1.1 V_{RHE} (Figure 3, Table S1), which was found to be the optimum potential for C₂ products in our previous studies on isolated Cu NCs synthesized by a similar approach.^{10,33} Figure 3a and Table S1 show that, independently on the size and shape of the Cu domain, the interface promotes CO₂RR over HER. Differences in product selectivity can then be ascribed to the Cu morphology before and/or after electrolysis (Figure S8). Noteworthy, the spherical 15 nm Cu NCs reconstruct towards cubes during electrolysis (Figure S8a), which explains the predominance of ethylene versus methane among the CO₂RR product.³⁴ The HDs with the 24 nm Cu domains have higher selectivity for ethylene while the HDs with the 36 nm and 54 nm Cu domains favour methane over ethylene. This difference in selectivity can be assigned to the Cu shape; indeed, the TEM analysis reported above and in the Supporting Information shows that the Cu domain in the Cu(24nm)/CeO_{2-x} HDs possess a more faceted cuboidal morphology, in contrast the Cu domain in the Cu(36nm)/CeO_{2-x} HDs and the Cu(54nm)/CeO_{2-x} HDs are more spherical.^{35,36} Considering the higher storage capacity of

multicarbon products and the interest in C-C coupling, the HDs with the cuboidal Cu domains of 24 nm were selected to investigate further the role of the interface.

The effect of loading (8 μg , 15 μg , 25 μg , 35 μg) on the electrocatalytic performance was investigated next (Figure S9). The results showed that the HDs always outperform the isolated Cu NCs and the Cu-CeO_{2-x} mix in terms of promoting CO₂RR versus HER. An increased C₂/C₁ product ratio and higher current were observed at higher loading, but also a simultaneous increase of HER. Such behaviour is consistent with mass transport effects accompanying a decreased inter-particle distance.³⁷ Thus, as a trade-off between activity and selectivity for CO₂RR products, one of the lower loading (15 μg) was chosen to proceed.

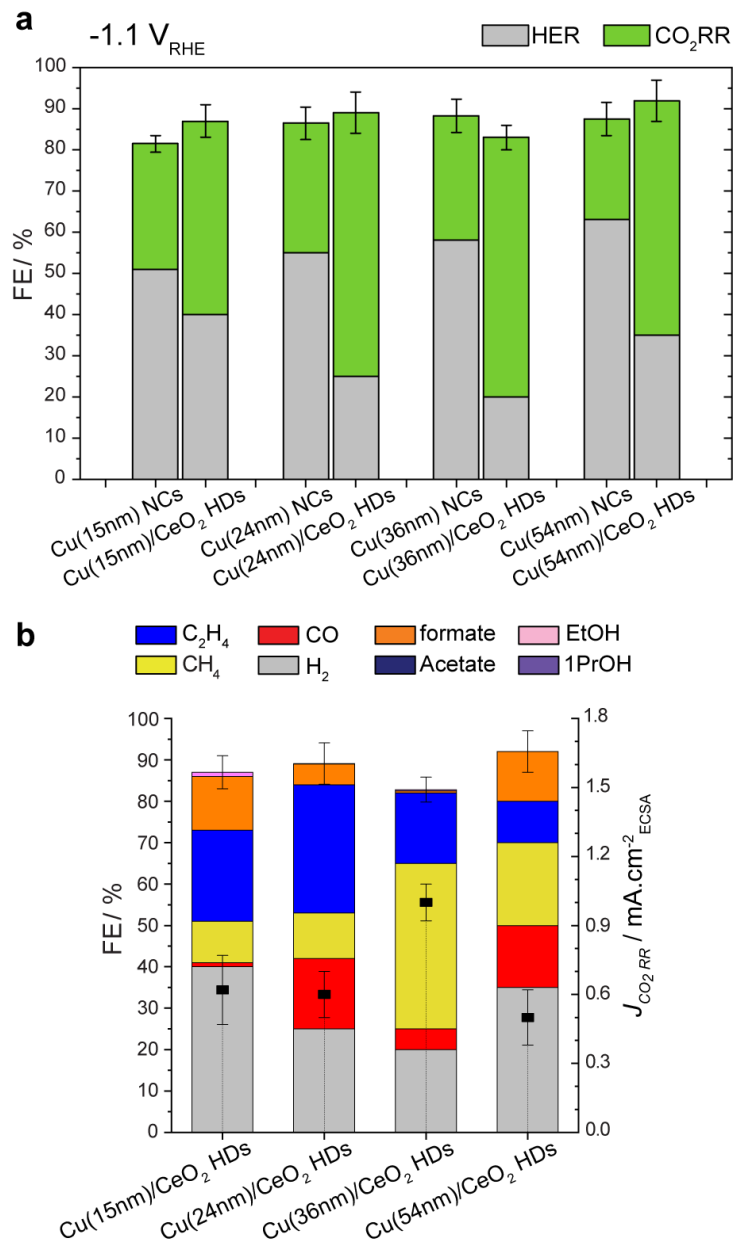


Figure 3. a) CO₂RR vs. HER selectivity for 15 μg of Cu/CeO_{2-x} HDs and bare Cu NCs with different Cu domain sizes. b) Faradaic efficiencies and CO₂RR partial current-densities for 15 μg of Cu/CeO_{2-x} HDs with different Cu domain sizes loaded on a glassy-carbon surface of 1 cm², measured at $-1.1 V_{\text{RHE}}$. The error bars correspond to the standard deviation from three independent measurements.

Figure 4 reports the faradaic efficiencies (FEs) of gaseous products at different potentials as well as their partial current-densities, normalized by the electrochemically-active surface area (ECSA, Figure S10). To start with lower potentials, hydrogen is observed as the dominant product in all samples, constituting more than 65% out of the total FE. By increasing the potential to $-1.1 \text{ V}_{\text{RHE}}$, a rise in the FE of $\text{C}_1\text{-C}_2$ products and a decrease of HER was noticed, especially remarkable in the case of HDs. Once the potential raises to $-1.2 \text{ V}_{\text{RHE}}$, the selectivity for methane is promoted in all the samples, but much significantly in the case of HDs (same statement applies to the HDs with different Cu domain size, Figure S11 and Table S1). Larger potentials ($-1.3 \text{ V}_{\text{RHE}}$) enhance the activity for H_2 while diminishing CO_2RR in all samples.

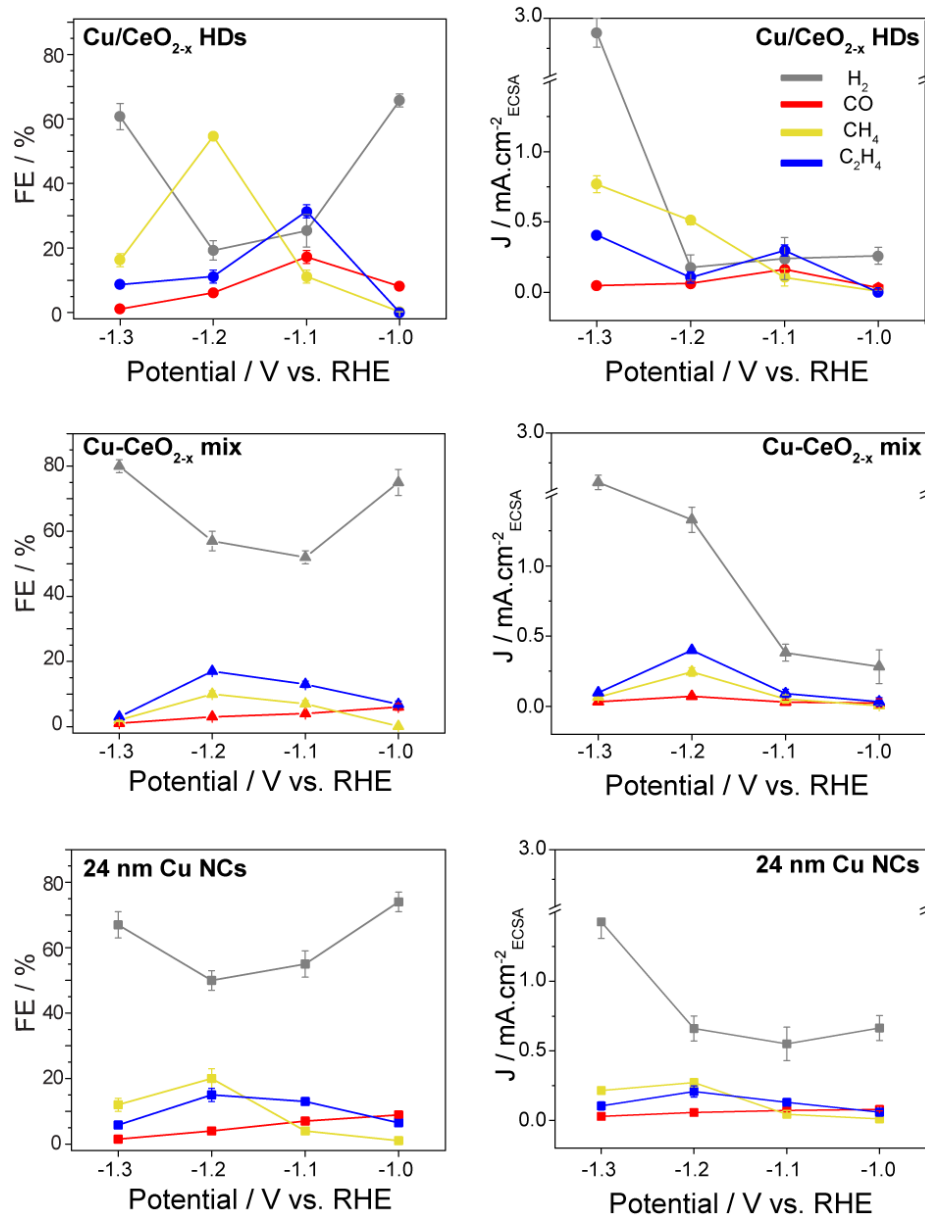


Figure 4. Faradaic efficiencies (left) and partial current densities (right) normalized by the ECSA for the gas products in Cu/CeO_{2-x} HDs, Cu-CeO_{2-x} mix and 24 nm Cu NCs at various applied potentials. The error bars correspond to the standard deviation from three independent measurements.

Figure 5 highlights the CO₂RR performance, including liquid products, of the above samples plus isolated CeO₂ NCs, measured at $-1.2 V_{\text{RHE}}$, where the HER contribution is minimal. The Cu/CeO_{2-x} HDs clearly outperform both the isolated NCs and the physical mixture in terms of selectivity towards CO₂RR, which reaches up to 80%. Furthermore, methane formation is greatly promoted with FE as high as 54%. These FE values are similar to those obtained for the above-mentioned study on Cu-doped CeO₂²², but here they are obtained at a remarkably lower potential ($-1.2 V_{\text{RHE}}$ in the Cu/CeO_{2-x} HDs versus $-1.8 V_{\text{RHE}}$ in the Cu-doped CeO₂). This result highlights the role of the unique interface obtained by employing the colloidal synthesis method. The intrinsic activity of Cu towards the CO₂RR improves only slightly in the presence of the CeO_{2-x} considering the subtle increase in the CO₂RR partial current-density when comparing the Cu NCs, the Cu-CeO_{2-x} mixture and the Cu/CeO_{2-x} HDs (Figure 5). We note that HDs with different Cu domain size were also tested at $-1.2 V_{\text{RHE}}$ (Figure S11) but the product distribution was almost similar in all of them. This result indicates that at higher applied potentials interface effects dominate over other all other parameters such as size and shape of the copper. Good stability was also observed in terms of activity and selectivity with preservation of the morphology and of interface, with the exception of the Cu(15nm)/CeO_{2-x} (Figure S8 and Figure S12).

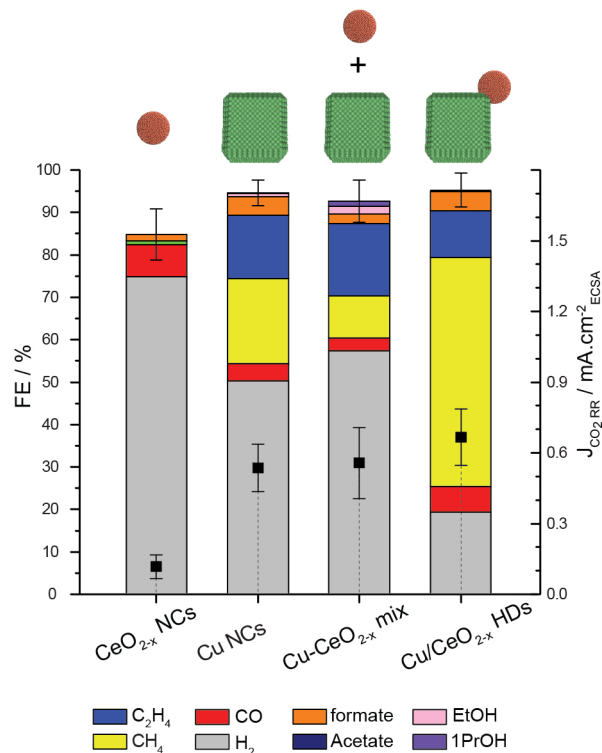


Figure 5. Faradic efficiencies and CO₂RR partial current-densities for 15 μg of Cu/CeO_{2-x} HDs, Cu-CeO_{2-x} mix, Cu NCs and CeO_{2-x} NCs loaded on a glassy-carbon surface of 1 cm², measured at $-1.2 \text{ V}_{\text{RHE}}$. The error bars indicate the standard deviation in the total FE. It is worth noting that the total FE in the CeO_{2-x} is less than 90%. Oxidation of some unaccounted formate and MeOH at the Pt anode has been reported to contribute to the lack of 100% total FE^{38,39}. Also, some electrons might be used for the formation of oxygen vacancies in CeO_{2-x}, thereby contributing to non-productive current.

The role of Ce³⁺ and oxygen vacancies are often called out to explain the catalytic behavior of metal/ceria catalysts.^{17,21,22} To examine the structural defects in the Cu/CeO_{2-x} HDs, X-ray photoelectron spectroscopy (XPS), UV-vis and Raman spectroscopy were performed (Figure 6). The XPS analysis (Figure 6a) shows that the HDs contain a higher fraction of Ce³⁺ when compared with the physical mixture, which appears very similar to the isolated CeO_{2-x} NCs. Concomitantly,

the fraction of oxidized Cu increases in the Cu/CeO_{2-x} HDs with respect to the Cu-CeO_{2-x} mix (Figure S13), indicating that these changes are interconnected. Oxygen vacancies (O_v) must accompany Ce³⁺ to maintain electro-neutrality in the lattice. Consistently with the XPS results, Raman spectroscopy (Figure 6b) reveals that the variation in the O_v concentration follows the same trends of the Ce³⁺ concentration when comparing the different samples, meaning higher O_v concentration in the Cu/CeO_{2-x} HDs. The observations regarding the oxidation state of Ce in the HDs were further confirmed by UV-vis absorption spectroscopy (Figure 6c). The absorption peaks located at 250 nm and 300 nm are assigned to Ce₂O₃ and CeO₂, respectively.^{40–42} The higher fraction of Ce³⁺ in the HDs triggers a blue-shift in its absorption profile while the absorption edge of the Cu-CeO_{2-x} mix and of the CeO_{2-x} NCs remained closer to the 300 nm. Being the only technique compatible with the glassy carbon support, XPS analysis was performed after electrocatalysis. The results in Figure 6a show an increase of the Ce³⁺ peak in all samples but more pronounced in the HDs. All together, these findings support the existence of a strong interfacial interaction between copper and ceria which boosts the migration of lattice oxygen across the interface and further assists the ceria domain to be reduced.^{43–45}

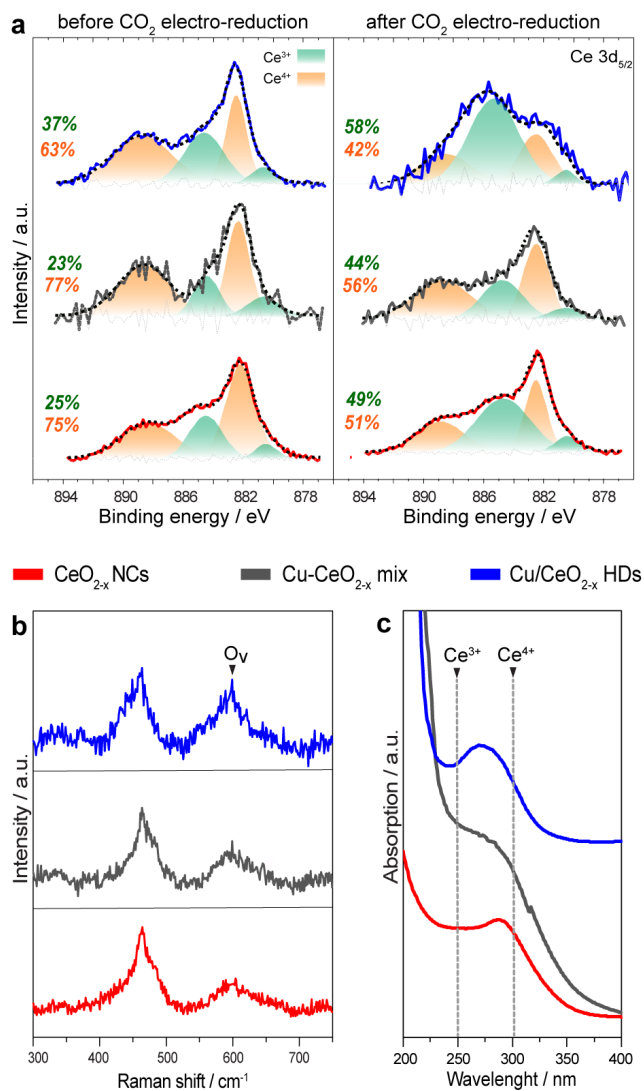


Figure 6. a) XPS spectra of the Ce 3d_{5/2} in Cu/CeO_{2-x} HDs, Cu-CeO_{2-x} mix and isolated CeO_{2-x} NCs before and after the full CO₂RR experiment (at -1.2 V_{RHE} for 80 min), where the solid lines indicate the experimental data and the dashed lines correspond to the fitting. The difference between them is reported at the bottom. b) Raman spectra normalized to the F_{2g} band of CeO_{2-x} at 462 cm⁻¹. c) UV-vis absorption spectra measured in hexane solutions.

In order to gain insights into the chemical state and structure of the Cu/CeO_{2-x} HDs during CO₂RR, operando X-ray absorption spectroscopy measurements were performed at -1.1 V_{RHE} and

-1.2 V_{RHE} in CO_2 -saturated 0.1 M KHCO_3 (Figure 7). Figures 7a and 7b show the temporal evolution of the X-ray absorption near-edge (XANES) spectra of $\text{Cu}(24\text{nm})/\text{CeO}_{2-x}$ HDs at the two potentials, measured at the Ce L_{III} -edge. Notably, the XANES spectrum of the pristine HDs show distinct differences with respect to reference CeO_2 pellet, with a broader absorption feature above the edge, so-called “white line”, indicating that the ceria domains of HDs are not completely oxidized and contain some Ce^{3+} species, which is consistent with our XPS, Raman and Uv-Vis results in Figure 6. The addition of the electrolyte didn’t change the state of the electrocatalyst. Upon starting the CO_2RR experiment, ceria undergoes a noticeable reduction as indicated by the shift of its white line toward Ce^{3+} . Figure 7c plots the weight fractions of Ce in its two different oxidation states at -1.1 V_{RHE} and -1.2 V_{RHE} . In both cases the relative reduction of Ce^{4+} to Ce^{3+} in the $\text{Cu}/\text{CeO}_{2-x}$ system occurs in the very early stages upon applying the negative potential, however the Ce reduction is faster -1.2 V_{RHE} , which is expected because of the more negative applied potential. After this initial change, the ratio of $\text{Ce}^{3+}/\text{Ce}^{4+}$ remains relatively constant, even when the potential is removed (last data point). This result confirms that the partial reduction of Ce^{4+} to Ce^{3+} is not reversible (indeed we can measure a similar ratio with ex-situ XPS). As for the XANES spectra of Cu (Figure S14), the metallic Cu remains unchanged during the whole reaction; whereas XPS analysis indicates that the oxidized surface of Cu domains in HDs gets partially reduced during CO_2RR (Figure S13).

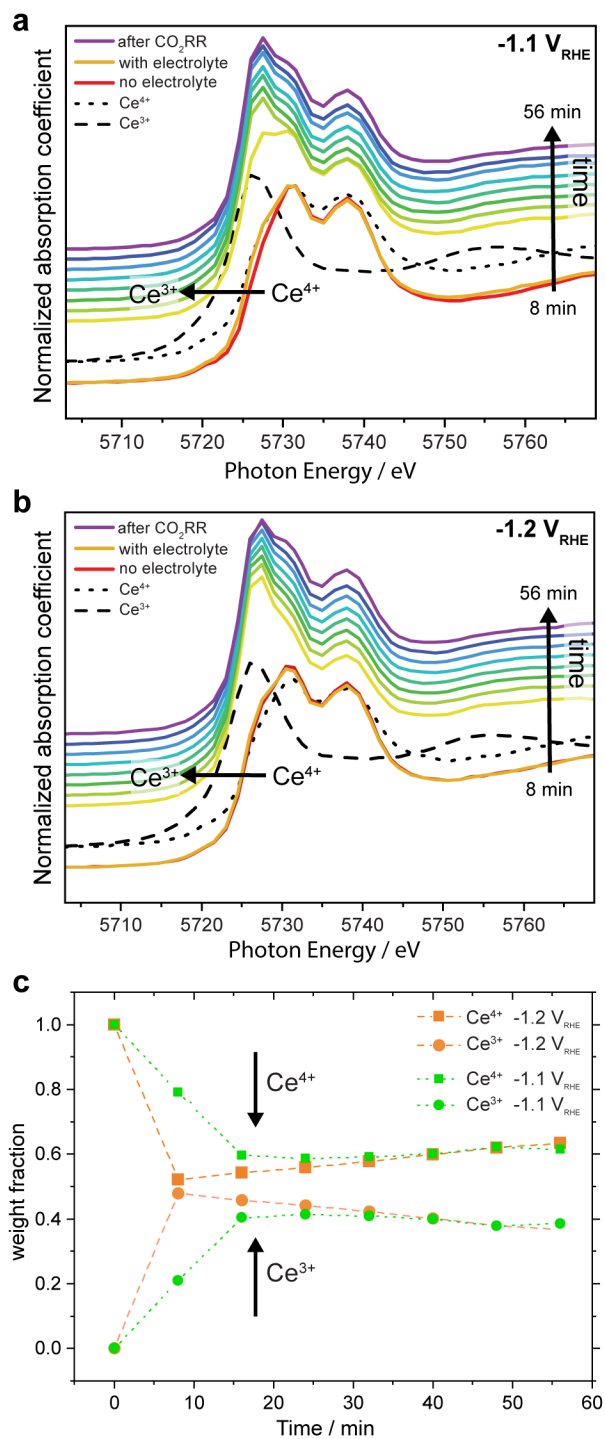


Figure 7. a) Ce L_{III}-edge XANES spectra measured on the as-prepared Cu/CeO_{2-x} HDs and under CO₂RR conditions at a) -1.1 V_{RHE} and b) -1.2 V_{RHE} in 0.1 M KHCO₃. The spectra were acquired

every 8 minutes. Reference spectra from CeO_2 powders and $\text{Ce}(\text{acetate})_3$ are also shown. c) Weighed spectra components versus electrolysis time at the two different potentials.

To model the interfacial interactions in the HDs, to map the reaction mechanism thereon and to understand the signatures of synergistic effects from first principles, we have used a ceria nanoparticle on Cu-slab representation inspired by Graciani et al.¹⁵ Results of the DFT calculations are reported in Figures 8 and 9 while details are provided in the Supporting Information (Tables S2, S3, S4). Computational hydrogen electrode model was used for evaluation of reaction thermodynamics of elementary proton transfer steps. The Cu(111) surface was chosen in the simulation model because of the results from HRTEM (Figure 2). In the model, the Bader charge-based oxidation state of Ce is +2.2 which is intermediate between that of Ce in bulk CeO_2 (+2.48) and Ce_2O_3 (+2.04). The binding between the cluster and the Cu-slab is chemisorption type, and we observe charge transfer from Cu atoms to the cluster. Cu atoms binding with O atoms of the cluster lose ~ 0.25 electrons each from their Bader volume. Two electrons are transferred to the top-most Cu layer. This analysis matches well with the spectroscopic studies on the as prepared sample reported in Figure 6 and provides confidence on the following simulation, which is based on the analysis of electronic structure under reaction condition. The Ce_6O_{13} cluster evolves with applied potential as the proton transfer reaction (hydrogenation of oxygen and O-vacancy creation) takes place. On application of the reducing potential ($-1.2 \text{ V}_{\text{RHE}}$), hydrogenation of all O atoms is spontaneous except the central oxygen atom buried between the cluster and the Cu-surface (Figure 8a). Further proton transfer leads to oxygen vacancy creation with the removal of oxygen. It is energetically favorable to form O-vacancies at the corner and top side of the cluster but not along the sides of the triangular shaped cluster. The final configuration of the cluster ($\text{Ce}_6\text{O}_7\text{H}_6$) stable at $-1.2 \text{ V}_{\text{RHE}}$ provides unique O-vacancy mediated active sites consisting of Ce atom (with O-

vacancy) and Cu atom. Charge transfer from Cu atoms coordinating with the cluster is further enhanced in reducing condition with those Cu-atoms losing ~ 0.4 electrons compared to an isolated Cu-slab. The ceria cluster accepts 6 electrons from the slab. Bader charge based oxidation state of Ce atoms range from +1.7 to +1.85. This is further reduction from that observed in Ce(III) oxide. The Cu d-band shifts to lower energy away from the Fermi level (Figure 8b). Following the d-band model for adsorption on metal surfaces, this change should weaken the binding energy at the Cu-coordinated site. The charge exchange map in Figure 8c shows the most significant relocation of Cu-electrons into the Ce atoms at the three corners of the cluster. These Ce atoms with low oxygen coordination are also possible adsorption sites for bidentate reaction intermediates, which can bind to both these Ce atoms and the nearest Cu atoms. Bidentate adsorbates are inherently more stable and thus define the reaction mechanism.

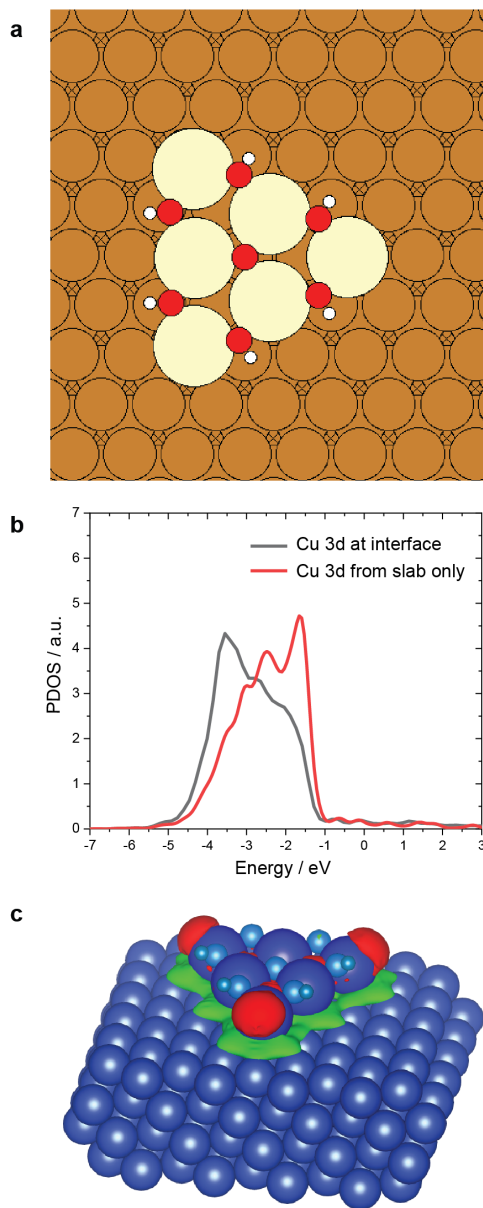


Figure 8. (a) Atomic configuration of CeO₂ cluster on Cu(111) surface at a reducing potential of $-1.2 V_{\text{RHE}}$ after successive reduction steps via protonation. (b) Partial density of states of the d-orbital of an interfacial Cu atom with and without CeO_{2-x} cluster being present (c) Charge exchange map between Cu(111) slab and CeO_{2-x} cluster calculated from charge density calculation of the whole system, Cu-slab only and cluster only. Red isosurface (+0.0015) is enrichment region and

green isosurface (-0.0015) signify depletion. For (a) and (c) Ce, Cu, O, H atoms are represented with blue spheres with sizes of following order Ce>Cu>O>H.

Moving towards to investigating the reactivity of the HDs, a full reaction tree network (Figure S15) was analyzed through a divide and conquer approach to select the most thermodynamically favorable pathway. The latter is illustrated in Figure 9a and the relative energetics in Figure 9b show that the bidentate adsorption of the CO₂ molecule through corner Ce atom and Cu atom stabilizes the adsorbed species such that gain in free energy for this chemical step is 55 meV. The first protonation step from CO₂ to COOH* is downhill by 0.47 eV. COOH* gets dissociated (barrier free) so that the C atom (of CO* part) binds to an interfacial Cu site and the O atom (of OH* part) binds to under-coordinated corner Ce (Figure 9a). Migration of this CO* from the interfacial Cu-site to another Cu-site on the slab lowers free energy by 0.92 eV. Thus, for surmountable kinetic barriers, the HDs produce a significant amount of surface bound CO* which are expected to cover the Cu-slab surface. CO* coverage especially impacts HER on copper surface. CO* coverage blocks active sites from HER as well as thwarts the HER activity by modifying H* binding energy through adsorbate-adsorbate interaction⁴⁶. The recently constructed HER volcano plot for metals in CO₂RR condition with CO* coverage⁴⁶, show that binding energy modification leads to suppression of HER. Cu sits in the right leg of the volcano plot. In addition to the CO* coverage effects on rest of the Cu-slab surface, interfacial Cu-sites have comparatively weaker binding energy as portrayed by the d-band position. This effect moves those Cu-sites further down the right leg of the aforementioned activity volcano. d-band shift is insignificant beyond the interfacial Cu-atoms, but stronger CO* binding enhances adsorbate-adsorbate interaction making HER suppression more significant.

The second electron transfer step in the CO₂RR mechanism (i.e. the protonation of interfacial Cu-site bound CO* which eventually leads to CHO*) requires a reducing potential of -0.45 eV. Subsequently, the OH* at Ce site is reduced to water leaving CHO* at the interfacial site for further reduction. This particular intermediate is unique for CO₂RR on Cu/CeO_{2-x} HD as CHO* binds through both a Cu-site and an O-vacancy site on Ce-atom, while CO* binds only on the Cu-site. The ensuing proton transfer leads to H₂CO*, which is also a bidentate adsorbate through O/C-atoms. The 5th reaction step involves protonation at the C-atom and H₃CO* thus formed is monodentate, binding only through O-atom to the Ce-site. Protonation of H₃CO* at C-atom leads to methane, and that at O atom leads to methanol release. CeO_{2-x} has high oxygen affinity in reduced condition, and it is difficult to cleave the Ce-O bond compared to C-O bond. We estimate the free energy difference between the formation of methanol and methane from H₃CO* to be over 2.3 eV. Due to universality of Brønsted-Evans-Polanyi relation^{47,48}, the kinetic barrier for formation of methanol is expected to be much higher than methane as well. This result clearly explains the observed selective evolution of methane. Release of methane leaves O atom at the Ce-site, which is removed as water through two proton transfer steps. Reaction thermodynamics shows that even at 0 V_{RHE}, only two elementary steps are free energy positive, specifically those where OH* bound to Ce-site is removed as water. Thus the onset potential limitation comes from OH* removal potential. This is in agreement with the reaction thermodynamics generally observed for oxide CO₂RR catalysts³¹. Achieving similar bidentate adsorption stabilization of other key intermediates which lowering the OH* binding energy will further improve the activity of HDs with another oxide domain in the future.

Previous theoretical studies on reaction mechanism and scaling relation based thermodynamic activity volcano analysis have shown that CO* protonation to CHO* is the limiting step. The low

slope of the CO*/CHO* adsorbate scaling law prohibits significant improvement over Cu catalysts for any other metallic system as the reaction mechanism stays unchanged. Workaround from this limitation has been proposed, including (a) metal oxide catalysts where a different reaction mechanism without CO*/CHO* intermediate being active might circumvent the scaling relation limitation^{31,49,50} and (b) doped metal chalcogenide 2D catalysts where CO* and CHO* binds through separate metallic and covalent site breaking the scaling relation⁵¹. Our study combines both these concepts through a design of special interfacial catalyst motif where CHO* is independently stabilized over CO*, thus deviating from the scaling relation (Figure 9c). CO*/CHO* scaling has been shown to be the bottleneck in CO₂RR activity for metallic catalysts⁵⁰ as it enforces large reducing potential for protonation of CO* to CHO*. Breaking of the scaling relation with additionally stable CHO* makes this reaction step facile at 0 V_{RHE} and thus removing this limitation. H₂CO* is also bidentate – deviating from the scaling line with OH* (Figure 9d). Also part of the reaction mechanism shifts to O-coordinated intermediate adsorbed through O-vacancy in oxide. The O-vacancy site coordinated H₃CO*, O* and OH* intermediate resembles the pathway active on oxide CO₂RR catalysts^{31,49,52}. These findings indicate a scientific breakthrough in designing CO₂RR catalysts by overcoming scaling law based limitations which will inspire CO₂RR researchers towards further systemic improvement in activity and selectivity.

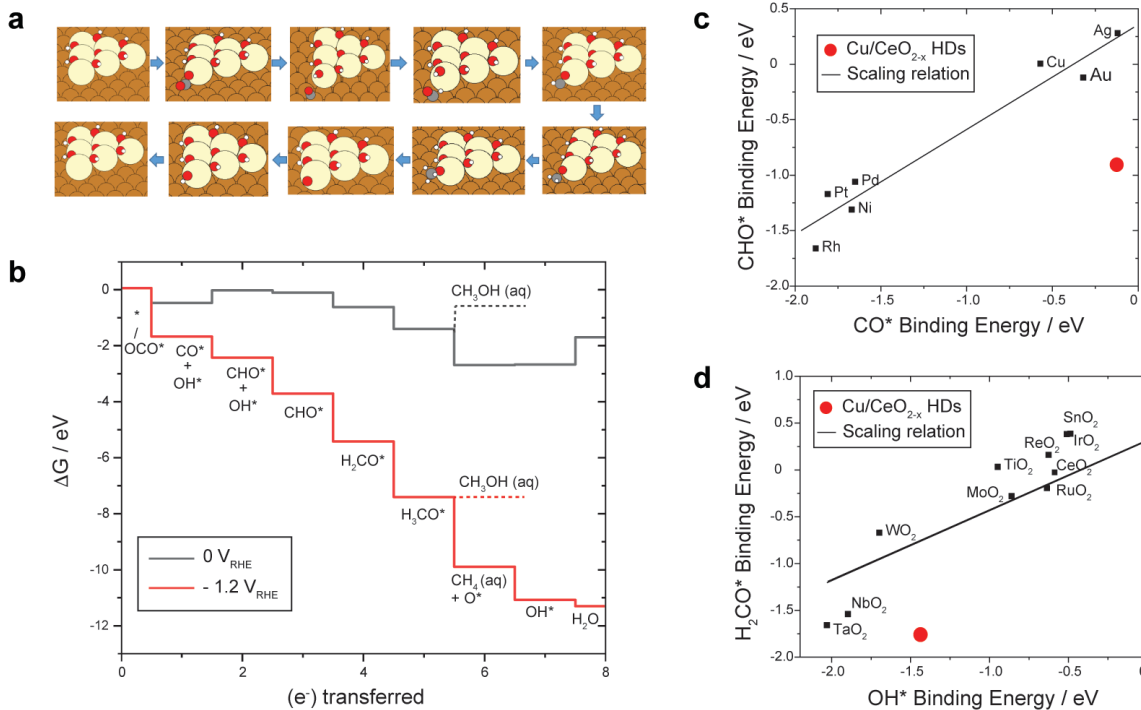


Figure 9. (a) CO₂RR mechanism on Cu/CeO_{2-x} HDs for methane evolution at the interfacial active sites. (b) Thermodynamics of methane and methanol evolution at 0 V_{RHE} and -1.2 V_{RHE} following this mechanism. (c,d) Breaking of CO*/CHO* and H₂CO*/OH* scaling relations due to additional through bidentate adsorption. Reference scaling relations from ⁵³ and ³¹

4 CONCLUSIONS

In conclusion, we have successfully synthesized nanocrystalline Cu/CeO_{2-x} HDs by developing a colloidal seeded-growth technique which allows to overcome the significant lattice mismatch between the two domains. The Cu/CeO_{2-x} interface affords synergistic properties, not observed by simply physically mixing the Cu and CeO_{2-x} NCs, which promote CO₂RR, in particular methane, and inhibit HER. This interface effect is explained by the formation of unique active sites at the interface which can stabilize CO₂RR intermediates through bidentate adsorption at both Cu and

CeO_{2-x} O-vacancy site thus allowing the opportunity for reaction engineering beyond scaling relationship limitations.

Our study on Cu/CeO_{2-x} highlights how multicomponent catalytic platforms can aid the discovery of new mechanisms to promote CO₂RR. The thermodynamics arising from the congregation of the oxide and metallic NCs provide direction towards further activity and selectivity improvement, for example by substituting the oxide domain.

Supporting information

The following files are available free of charge on ACS Publication Website.

Experimental procedures, TEM images, XRD patterns, electrocatalytic measurements, XPS data, XANES data, DFT tables.

Acknowledgements

This work was primarily supported by the European Research Council under Starting Grant ERC-HYCAT with agreement number 715634. Arghya Bhowmik acknowledge financial support from VILLUM FONDEN by a research grant (00023105) for DeepDFT project. The authors thank Dr. James R. Pankhurst for his help in the electrochemical surface area measurements and critical reading of the manuscript, Dr. Anna Loiudice for comments on the manuscript. The authors acknowledge the Paul Scherrer Institut, Villigen, Switzerland for provision of synchrotron radiation beamtime at beamline SuperXAS of the SLS and would like to thank Dr. Grigory Smolentsev for assistance.

References

- (1) Seh, Z. W.; Kibsgaard, J.; Dickens, C. F.; Chorkendorff, I.; Nørskov, J. K.; Jaramillo, T. F. Combining Theory and Experiment in Electrocatalysis: Insights into Materials Design. *Science* **2017**, *355* (6321), eaad4998.
- (2) Larrazábal, G. O.; Martín, A. J.; Pérez-Ramírez, J. Building Blocks for High Performance in Electrocatalytic CO₂ Reduction: Materials, Optimization Strategies, and Device Engineering. *J. Phys. Chem. Lett.* **2017**, *8* (16), 3933–3944.
- (3) Kuhl, K. P.; Cave, E. R.; Abram, D. N.; Jaramillo, T. F. New Insights into the Electrochemical Reduction of Carbon Dioxide on Metallic Copper Surfaces. *Energy Environ. Sci.* **2012**, *5* (5), 7050.
- (4) Hansen, H. A.; Varley, J. B.; Peterson, A. A.; Nørskov, J. K. Understanding Trends in the Electrocatalytic Activity of Metals and Enzymes for CO₂ Reduction to CO. *J. Phys. Chem. Lett.* **2013**, *4* (3), 388–392.
- (5) Ulissi, Z. W.; Medford, A. J.; Bligaard, T.; Nørskov, J. K. To Address Surface Reaction Network Complexity Using Scaling Relations Machine Learning and DFT Calculations. *Nat. Commun.* **2017**, *8*, 14621.
- (6) Reske, R.; Mistry, H.; Behafarid, F.; Roldan Cuenya, B.; Strasser, P. Particle Size Effects in the Catalytic Electroreduction of CO₂ on Cu Nanoparticles. *J. Am. Chem. Soc.* **2014**, *136* (19), 6978–6986.
- (7) Manthiram, K.; Beberwyck, B. J.; Alivisatos, A. P. Enhanced Electrochemical Methanation of Carbon Dioxide with a Dispersible Nanoscale Copper Catalyst. *J. Am. Chem. Soc.* **2014**,

136 (38), 13319–13325.

- (8) Ma, M.; Djanashvili, K.; Smith, W. A. Controllable Hydrocarbon Formation from the Electrochemical Reduction of CO₂ over Cu Nanowire Arrays. *Angew. Chemie Int. Ed.* **2016**, 55 (23), 6680–6684.
- (9) Jeon, H. S.; Kunze, S.; Scholten, F.; Roldan Cuenya, B. Prism-Shaped Cu Nanocatalysts for Electrochemical CO₂ Reduction to Ethylene. *ACS Catal.* **2018**, 8 (1), 531–535.
- (10) Loiudice, A.; Lobaccaro, P.; Kamali, E. A.; Thao, T.; Huang, B. H.; Ager, J. W.; Buonsanti, R. Tailoring Copper Nanocrystals towards C₂ Products in Electrochemical CO₂ Reduction. *Angew. Chemie Int. Ed.* **2016**, 55 (19), 5789–5792.
- (11) Li, Y.; Cui, F.; Ross, M. B.; Kim, D.; Sun, Y.; Yang, P. Structure-Sensitive CO₂ Electroreduction to Hydrocarbons on Ultrathin 5-Fold Twinned Copper Nanowires. *Nano Lett.* **2017**, 17 (2), 1312–1317.
- (12) Clark, E. L.; Hahn, C.; Jaramillo, T. F.; Bell, A. T. Electrochemical CO₂ Reduction over Compressively Strained CuAg Surface Alloys with Enhanced Multi-Carbon Oxygenate Selectivity. *J. Am. Chem. Soc.* **2017**, 139 (44), 15848–15857.
- (13) Kim, D.; Resasco, J.; Yu, Y.; Asiri, A. M.; Yang, P. Synergistic Geometric and Electronic Effects for Electrochemical Reduction of Carbon Dioxide Using Gold–Copper Bimetallic Nanoparticles. *Nat. Commun.* **2014**, 5 (1), 4948.
- (14) Huang, J.; Mensi, M.; Oveisi, E.; Mantella, V.; Buonsanti, R. Structural Sensitivities in Bimetallic Catalysts for Electrochemical CO₂ Reduction Revealed by Ag–Cu Nanodimers. *J. Am. Chem. Soc.* **2019**, 141 (6), 2490–2499.

- (15) Zhou, Y.; Che, F.; Liu, M.; Zou, C.; Liang, Z.; De Luna, P.; Yuan, H.; Li, J.; Wang, Z.; Xie, H.; et al. Dopant-Induced Electron Localization Drives CO₂ Reduction to C₂ Hydrocarbons. *Nat. Chem.* **2018**, *10* (9), 974–980.
- (16) Kattel, S.; Liu, P.; Chen, J. G. Tuning Selectivity of CO₂ Hydrogenation Reactions at the Metal/Oxide Interface. *J. Am. Chem. Soc.* **2017**, *139* (29), 9739–9754.
- (17) Graciani, J.; Mudiyansele, K.; Xu, F.; Baber, A. E.; Evans, J.; Senanayake, S. D.; Stacchiola, D. J.; Liu, P.; Hrbek, J.; Fernández Sanz, J.; et al. Highly Active Copper-Ceria and Copper-Ceria-Titania Catalysts for Methanol Synthesis from CO₂. *Science* (80-.). **2015**, *345* (6196), 546–550.
- (18) Cargnello, M.; Doan-Nguyen, V. V. T.; Gordon, T. R.; Diaz, R. E.; Stach, E. A.; Gorte, R. J.; Fornasiero, P.; Murray, C. B. Control of Metal Nanocrystal Size Reveals Metal-Support Interface Role for Ceria Catalysts. *Science* **2013**, *341* (6147), 771–773.
- (19) Montini, T.; Melchionna, M.; Monai, M.; Fornasiero, P. Fundamentals and Catalytic Applications of CeO₂-Based Materials. *Chem. Rev.* **2016**, *116* (10), 5987–6041.
- (20) Yang, S.-C.; Pang, S. H.; Sulmonetti, T. P.; Su, W.-N.; Lee, J.-F.; Hwang, B.-J.; Jones, C. W. Synergy between Ceria Oxygen Vacancies and Cu Nanoparticles Facilitates the Catalytic Conversion of CO₂ to CO under Mild Conditions. *ACS Catal.* **2018**, *8* (12), 12056–12066.
- (21) Gao, D.; Zhang, Y.; Zhou, Z.; Cai, F.; Zhao, X.; Huang, W.; Li, Y.; Zhu, J.; Liu, P.; Yang, F.; et al. Enhancing CO₂ Electroreduction with the Metal–Oxide Interface. *J. Am. Chem. Soc.* **2017**, *139* (16), 5652–5655.

- (22) Wang, Y.; Chen, Z.; Han, P.; Du, Y.; Gu, Z.; Xu, X.; Zheng, G. Single-Atomic Cu with Multiple Oxygen Vacancies on Ceria for Electrocatalytic CO₂ Reduction to CH₄. *ACS Catal.* **2018**, 8 (8), 7113–7119.
- (23) Li, Q.; Fu, J.; Zhu, W.; Chen, Z.; Shen, B.; Wu, L.; Xi, Z.; Wang, T.; Lu, G.; Zhu, J.; et al. Tuning Sn-Catalysis for Electrochemical Reduction of CO₂ to CO via the Core/Shell Cu/SnO₂ Structure. *J. Am. Chem. Soc.* **2017**, 139 (12), 4290–4293.
- (24) Huo, S.; Weng, Z.; Wu, Z.; Zhong, Y.; Wu, Y.; Fang, J.; Wang, H. Coupled Metal/Oxide Catalysts with Tunable Product Selectivity for Electrocatalytic CO₂ Reduction. *ACS Appl. Mater. Interfaces* **2017**, 9 (34), 28519–28526.
- (25) Andrews, E.; Ren, M.; Wang, F.; Zhang, Z.; Sprunger, P.; Kurtz, R.; Flake, J. Electrochemical Reduction of CO₂ at Cu Nanocluster / (100) ZnO Electrodes. *J. Electrochem. Soc.* **2013**, 160 (11), H841–H846.
- (26) Casavola, M.; Buonsanti, R.; Caputo, G.; Cozzoli, P. D. Colloidal Strategies for Preparing Oxide-Based Hybrid Nanocrystals. *Eur. J. Inorg. Chem.* **2008**, 2008 (6), 837–854.
- (27) Buonsanti, R.; Grillo, V.; Carlino, E.; Giannini, C.; Curri, M. L.; Innocenti, C.; Sangregorio, C.; Klaus Achterhold; Fritz Günter Parak; Angela Agostiano, A.; et al. Seeded Growth of Asymmetric Binary Nanocrystals Made of a Semiconductor TiO₂ Rodlike Section and a Magnetic γ -Fe₂O₃ Spherical Domain. *J. Am. Chem. Soc.* **2006**, 128 (51), 16953–16970.
- (28) Kresse, G. From Ultrasoft Pseudopotentials to the Projector Augmented-Wave Method. *Phys. Rev. B* **1999**, 59 (3), 1758–1775.
- (29) Hjorth Larsen, A.; Jørgen Mortensen, J.; Blomqvist, J.; Castelli, I. E.; Christensen, R.;

- Duřak, M.; Friis, J.; Groves, M. N.; Hammer, B.; Hargus, C.; et al. The Atomic Simulation Environment—a Python Library for Working with Atoms. *J. Phys. Condens. Matter* **2017**, *29* (27), 273002.
- (30) Hammer, B.; Hansen, L. B.; Nørskov, J. K. Improved Adsorption Energetics within Density-Functional Theory Using Revised Perdew-Burke-Ernzerhof Functionals. *Phys. Rev. B* **1999**, *59* (11), 7413–7421.
- (31) Bhowmik, A.; Vegge, T.; Hansen, H. A. Descriptors and Thermodynamic Limitations of Electrocatalytic Carbon Dioxide Reduction on Rutile Oxide Surfaces. *ChemSusChem* **2016**, *9* (22), 3230–3243.
- (32) Nørskov, J. K.; Rossmeisl, J.; Logadottir, A.; Lindqvist, L.; Kitchin, J. R.; Bligaard, T.; Jónsson, H. Origin of the Overpotential for Oxygen Reduction at a Fuel-Cell Cathode. *J. Phys. Chem. B* **2004**, *108* (46), 17886–17892.
- (33) Huang, J.; Hörmann, N.; Oveisi, E.; Loiudice, A.; De Gregorio, G. L.; Andreussi, O.; Marzari, N.; Buonsanti, R. Potential-Induced Nanoclustering of Metallic Catalysts during Electrochemical CO₂ Reduction. *Nat. Commun.* **2018**, *9* (1), 3117.
- (34) Kim, D.; Kley, C. S.; Li, Y.; Yang, P. Copper Nanoparticle Ensembles for Selective Electroreduction of CO₂ to C₂-C₃ Products. *Proc. Natl. Acad. Sci. U. S. A.* **2017**, *114* (40), 10560–10565.
- (35) Li, H.; Li, Y.; Koper, M. T. M.; Calle-Vallejo, F. Bond-Making and Breaking between Carbon, Nitrogen, and Oxygen in Electrocatalysis. *J. Am. Chem. Soc.* **2014**, *136* (44), 15694–15701.

- (36) Jan Schouten, K. P.; Qin, Z.; Pe, E.; Gallent, rez; M Koper, M. T. Two Pathways for the Formation of Ethylene in CO Reduction on Single-Crystal Copper Electrodes. *J. Am. Chem. Soc* **2012**, *134*, 15.
- (37) Mistry, H.; Behafarid, F.; Reske, R.; Varela, A. S.; Strasser, P.; Roldan Cuenya, B. Tuning Catalytic Selectivity at the Mesoscale via Interparticle Interactions. *ACS Catal.* **2016**, *6* (2), 1075–1080.
- (38) Gabardo, C. M.; Seifitokaldani, A.; Edwards, J. P.; Dinh, C.-T.; Burdyny, T.; Kibria, M. G.; O'Brien, C. P.; Sargent, E. H.; Sinton, D. Combined High Alkalinity and Pressurization Enable Efficient CO₂ Electroreduction to CO. *Energy Environ. Sci.* **2018**, *11* (9), 2531–2539.
- (39) Chen, Y. X.; Miki, A.; Ye, S.; Sakai, H.; Osawa, M. Formate, an Active Intermediate for Direct Oxidation of Methanol on Pt Electrode. *J. Am. Chem. Soc.* **2003**, *125* (13), 3680–3681.
- (40) Gao, W.; Zhang, Z.; Li, J.; Ma, Y.; Qu, Y. Surface Engineering on CeO₂ Nanorods by Chemical Redox Etching and Their Enhanced Catalytic Activity for CO Oxidation. *Nanoscale* **2015**, *7* (27), 11686–11691.
- (41) Yang, Y.; Mao, Z.; Huang, W.; Liu, L.; Li, J.; Li, J.; Wu, Q. Redox Enzyme-Mimicking Activities of CeO₂ Nanostructures: Intrinsic Influence of Exposed Facets. *Sci. Rep.* **2016**, *6* (1), 35344.
- (42) Hay, P. J.; Martin, R. L.; Uddin, J.; Scuseria, G. E. Theoretical Study of CeO₂ and Ce₂O₃ Using a Screened Hybrid Density Functional. *J. Chem. Phys.* **2006**, *125* (3), 034712.

- (43) Duchoň, T.; Dvořák, F.; Aulická, M.; Stetsovych, V.; Vorokhta, M.; Mazur, D.; Veltruská, K.; Skála, T.; Mysliveček, J.; Matolínová, I.; et al. Ordered Phases of Reduced Ceria As Epitaxial Films on Cu(111). *J. Phys. Chem. C* **2014**, *118* (1), 357–365.
- (44) Szabová, L.; Skála, T.; Matolínová, I.; Fabris, S.; Farnesi Camellone, M.; Matolín, V. Copper-Ceria Interaction: A Combined Photoemission and DFT Study. *Appl. Surf. Sci.* **2013**, *267*, 12–16.
- (45) Szabová, L.; Stetsovych, O.; Dvořák, F.; Farnesi Camellone, M.; Fabris, S.; Mysliveček, J.; Matolín, V. Distinct Physicochemical Properties of the First Ceria Monolayer on Cu(111). *J. Phys. Chem. C* **2012**, *116* (11), 6677–6684.
- (46) Cave, E. R.; Shi, C.; Kuhl, K. P.; Hatsukade, T.; Abram, D. N.; Hahn, C.; Chan, K.; Jaramillo, T. F. Trends in the Catalytic Activity of Hydrogen Evolution during CO₂ Electroreduction on Transition Metals. *ACS Catal.* **2018**, *8* (4), 3035–3040.
- (47) Wang, S.; Temel, B.; Shen, J.; Jones, G.; Grabow, L. C.; Studt, F.; Bligaard, T.; Abild-Pedersen, F.; Christensen, C. H.; Nørskov, J. K. Universal Brønsted-Evans-Polanyi Relations for C-C, C-O, C-N, N-O, N-N, and O-O Dissociation Reactions. *Catal. Letters* **2011**, *141* (3), 370–373.
- (48) Bligaard, T.; Nørskov, J. K.; Dahl, S.; Matthiesen, J.; Christensen, C. H.; Sehested, J. The Brønsted–Evans–Polanyi Relation and the Volcano Curve in Heterogeneous Catalysis. *J. Catal.* **2004**, *224* (1), 206–217.
- (49) Bhowmik, A.; Hansen, H. A.; Vegge, T. Electrochemical Reduction of CO₂ on Ir_xRu_(1-x)O₂ (110) Surfaces. *ACS Catal.* **2017**, *7* (12), 8502–8513.

- (50) Bhowmik, A.; Hansen, H. A.; Vegge, T. Role of CO* as a Spectator in CO₂ Electroreduction on RuO₂. *J. Phys. Chem. C* **2017**, *121* (34), 18333–18343.
- (51) Hong, X.; Chan, K.; Tsai, C.; Nørskov, J. K. How Doped MoS₂ Breaks Transition-Metal Scaling Relations for CO₂ Electrochemical Reduction. *ACS Catal.* **2016**, *6* (7), 4428–4437.
- (52) Karamad, M.; Hansen, H. A.; Rossmeisl, J.; Nørskov, J. K. Mechanistic Pathway in the Electrochemical Reduction of CO₂ on RuO₂. *ACS Catal.* **2015**, *5* (7), 4075–4081.
- (53) Shi, C.; Hansen, H. a; Lausche, A. C.; Nørskov, J. K. Trends in Electrochemical CO₂ Reduction Activity for Open and Close-Packed Metal Surfaces. *Phys. Chem. Chem. Phys.* **2014**, *16* (10), 4720–4727.